International Journal of Coal Science & Technology (2022) 9:12
https://doi.org/10.1007/s40789-022-00483-3

RESEARCH

Web pillar stability in open-pit highwall mining

Juyu Jiang[1] · Zhuowei Zhang[1] · Dong Wang[1] · Laigui Wang[1] · Xinping Han[1]

Received: 28 August 2021 / Accepted: 8 February 2022

Abstract
When highwall mining technology is applied to recover large amounts of residual coal left under the highwall of a big open-pit mine, a reasonable coal pillar width is required to ensure the stability of the web pillars. Using numerical simulations, this paper studied the characteristics of the abutment stress distribution in the web pillars under different slope angles and mining depths, and established a relation describing the stress distribution in the web pillar. The relationship between the abutment stress and the ultimate strength of the web pillar under different pillar widths was also analyzed. In combination with the failure characteristics of the pillar yield zone, this relationship was used to explore the instability mechanism of web pillars. Finally, the optimal retaining widths of the web pillars were determined. Based on the modeling results, a mechanical bearing model of the web pillar was established and a cusp catastrophe model of pillar-overburden was constructed. Additionally, the web pillar instability criterion was derived. By analyzing the ultimate strength of the web pillars, a formula for calculating the yield zone width either side of the pillars was established. Using the instability criterion of web pillars in highwall mining, a reasonable pillar width can be deduced theoretically, providing significant guidance on the application of highwall mining technology.

Keywords Open-pit mine · Highwall mining · Instability criterion · Web pillar · Coal pillar width

1 Introduction

China's coal resources are abundant, with demonstrated coal reserves that account for approximately 11.1% of global reserves (Wang et al. 2019a). Open-pit mining is an important technique for recovering coal resources, and has advantages such as safe operation, large output, environmental efficiency, good working conditions, and high mining intensity. Recently, open-pit mining has developed rapidly and its application is becoming increasingly widespread. In China, the proportion of open-pit coal mining has grown from 4% in the early 1990s to 16.2% in 2010 (Song et al. 2016). Although the advantages of open-pit mining have been highlighted in actual engineering practice, this method often leaves a large amount of residual coal that cannot be recovered (Zhao et al. 2020a, b). The advent of the LDC100 highwall miner provides an effective approach for recovering this residual coal in the highwall.

The highwall miner is a new open-pit highwall mining technology that combines the advantages of open-pit mining and underground mining to achieve highwall mining in soft and thick coal seams (Sasaoka et al. 2016; Ross et al. 2019). The mining and transporting process is fully automatic and remotely controlled (Wang et al. 2019b), allowing unmanned intelligent mining and transportation operations to be carried out in the coal chamber. In the highwall mining process, web pillars are set up between the chambers to support the overlying strata and prevent landslides, the burial of equipment, and other disasters (Wang et al. 2019c; Huang et al. 2021). When the web pillars become partially unstable, a chain of instability may be induced in the pillar group. This results in slope instability and landslides (Chandar et al. 2014, 2015), which endanger the safety of mining equipment and cause substantial loss of resources. Therefore, the stability of web pillars should be investigated and a reasonable web pillar size should be designed.

Globally, current research on web pillar stability in open-pit mining is mainly based on empirical formulas describing the coal pillar strength to determine the width of the web pillar (Bunting et al. 1911; Greenwald et al. 1939; Holland et al. 1957, 1964; Salamon et al. 1967; Bieniawski

✉ Juyu Jiang
jiangjuyu@lntu.edu.cn

[1] College of Mines, Liaoning Technical University, Fuxin 123000, Liaoning, China

Published online: 10 March 2022

et al. 1968; Sheorey 1992; Galvin et al. 1999). Porarthur et al. adopted hybrid empirical and numerical modeling techniques for web pillar design in India, and proposed the introduction of a correction factor into the empirical pillar strength equation for slender pillars with a width to height ratio of less than unity. This enabled a more reasonable design of the coal pillar parameters to be achieved (Porarthur et al. 2013). Lukáš et al. (2017) used rockbolt supports to address the issue of coal pillar stability and stabilization, and sufficiently reinforced several existing pillars. Deliveris and Benardos (2017) investigated approximate solutions using two-dimensional (2D) numerical simulation techniques and three-dimensional (3D) numerical analyses, and evaluated the geomechanical responses of the lignite pillar formed by the room and pillar mining method. They pointed out that 2D approximation techniques adequately approximate the actual 3D problem. Hikaru et al. (2013) considered the recovery ratio and used numerical analysis to develop an appropriate design for the width of the web coal pillar. Zhang et al. (2011) used the FLAC^{3D} (Fast Lagrangian Analysis of Continua in Three Dimensions; Itasca Consulting Group Inc., Minneapolis, Minnesota, USA) numerical simulation software to systematically investigate the laws governing the stress increase coefficient of the coal pillar and the pillar's stability. They obtained a function describing the relationships among the stress increase coefficient of the upper and lower pillars, the properties of the interstratified rock, and the geometrical parameters.

However, the results obtained in the abovementioned studies are not necessarily suitable for the geological conditions and the occurrence of coal and rock in China. Notably, the quality of coal in most parts of China is soft. Moreover, previous studies have not provided a detailed description of the instability mechanism or a reasonable instability criterion for the web pillar. As a result, the designed width of the web pillar is not necessarily reliable (Jiang et al. 2021). Therefore, taking an open-pit coal mine in Inner Mongolia, China, as the engineering geological background, this paper systematically studies the instability mechanism and the web pillar width by means of experimental analysis, numerical simulations, and cusp catastrophe theory. Our results are expected to provide a basis for the design and safety implementation of highwall mining schemes, as well as guidance for similar projects.

2 Engineering background

This paper focuses on the geological background of an open-pit mine located in Inner Mongolia Province, China. The strike length of the mine is 5.1 km. Two main coal seams, numbered 19 and 21, contain high-quality lignite. The expected advance length of the open cut operations is 360 m per year, and it is necessary to cut the coal in the No. 21 seam along the seam floor to allow for reasonable internal coal transport. The tracking distance of the internal transport is 50 m. The strata at the west end-slope of the open-pit mine are almost horizontally distributed, and there is no obvious change in lithology along the strike direction. The slope strata consists of surface soil, gritstone, siltstone, coal, and base sandstone from top to bottom (Fig. 1).

The LDC100 highwall miner (Han et al. 2014) is used to extract the coal left under the west highwall of the open-pit mine. This is an unmanned mining machine with a production capacity of 60 t/h and a suited coal-rock hardness factor of $f \leq 2$, which is applicable for recovery from lignite open-pit mines. The recovery chamber has a rectangular cross-section measuring 2 m (width) × 2.5 m (height). The maximum mining depth is 100 m and the mining process can be completed once every 3 days. The mechanical properties of the rocks and soil mass at the highwall of the open-pit mine are listed in Table 1.

3 Numerical modeling of the instability mechanism of web pillars

3.1 Model construction and experiment schemes

Taking the west highwall of an open-pit coal mine in Inner Mongolia as the engineering background, numerical simulation models of the web pillars under four slope angles (i.e., 20°, 30°, 40°, and 50°) are established separately using the finite difference modeling software FLAC^{3D}. These models allow the instability mechanism of web pillars to be studied at different slope angles and mining depths. The models represent the geological conditions around the target area shown in Fig. 1. To eliminate the boundary effect, coal pillars with a width of 60 m are retained at each side of the chambers, based on the theory of elastic–plastic mechanics (Ghaednia et al. 2017). As the element size has a great impact on the modeling results (Mo et al. 2018), the meshing elements in the target area should be precisely arranged to minimize

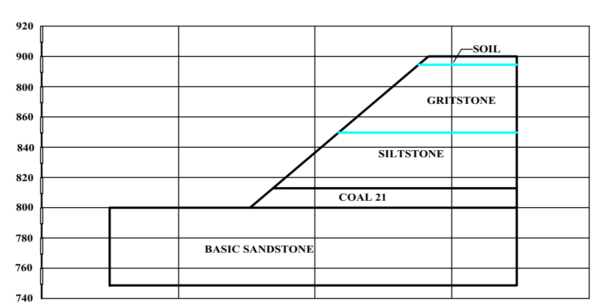

Fig. 1 Schematic diagram of lithology distribution of slope strata

Table 1 Mechanical properties of the rocks and soil mass

Strata formation	Compressive strength (MPa)	Tensile strength (MPa)	Cohesion (MPa)	Friction angle (°)	Elasticity modulus (GPa)	Poisson's ratio	Density (kg/m^3)
Sandstone	45.19	3.40	2.18	23	15.16	0.22	2010
No. 21 coal seam	17.66	2.06	0.30	17.6	7.41	0.29	1270
Siltstone	25.76	3.02	2.35	25	14.58	0.21	2090
Gritstone	51.43	4.90	2.12	22	15.62	0.21	1990
Soil	9.49	1.34	0.24	20	5.69	0.30	2671

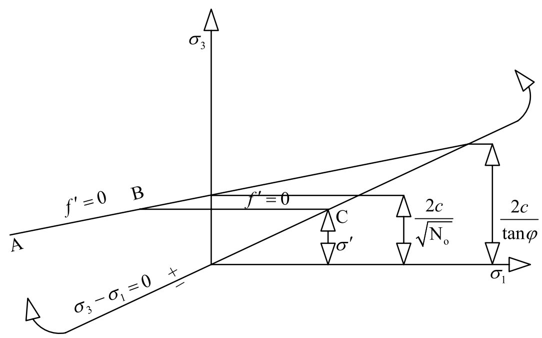

Fig. 2 Mohr–Coulomb failure criterion

Table 2 Simulated web pillar widths (m) under different mining depths (m) at slope angle 20°

Mining depth	Pillar width size I	Pillar width size II	Pillar width size III	Pillar width size IV
50	3.7	3.9	4.1	4.3
65	3.8	4.0	4.2	4.4
80	3.9	4.1	4.3	4.5
100	4.1	4.3	4.5	4.7

Table 3 Simulated web pillar widths (m) under different mining depths (m) at slope angle 30°

Mining depth	Pillar width size I	Pillar width size II	Pillar width size III	Pillar width size IV
50	3.9	4.1	4.3	4.5
65	4.1	4.3	4.5	4.7
80	4.3	4.5	4.7	4.9
100	4.6	4.8	5.0	5.2

Table 4 Simulated web pillar widths (m) under different mining depths (m) at slope angle 40°

Mining depth	Pillar width size I	Pillar width size II	Pillar width size III	Pillar width size IV
50	4.1	4.3	4.5	4.7
65	4.4	4.6	4.8	5.0
80	4.7	4.9	5.1	5.3
100	5.1	5.3	5.5	5.7

the influence of numerical errors. The element width was set to be 1 m along the pillar strike direction. Ten elements were set in each horizontal and vertical direction of the pillar cross-section. A total of 100 elements are used to discretize the pillar area. Horizontal constraints are imposed on both sides of the model, that is, the horizontal displacement was set to be zero, and the base boundary of the model was fixed, which means the horizontal and vertical displacements of the base boundary are both zero. The top surface and the slope face of the model are free boundaries. The loading stress is gravity, and the Mohr–Coulomb elastic–plastic constitutive model is used for calculation and analysis. The failure criteria used in the Mohr–Coulomb model are the Mohr–Coulomb failure criterion and the maximum tensile stress criterion. The relationship between the three principal stresses is $\sigma_1 \le \sigma_2 \le \sigma_3$; the failure criterion in the (σ_1, σ_3) plane is represented in Fig. 2.

According to the specifications of the LDC100 highwall miner, the chamber measures 2.5 m in height ($h = 2.5$ m) and 2 m in width ($a = 2$ m); the maximum mining depth is 100 m ($l = 100$ m), and one mining process can be completed in 3 days. As the slope angle and mining depth increase, the thickness of the overburden gradually increases, and the bearing stress of the coal pillar increases. A larger pillar width provides greater ultimate strength. At larger values of the slope angle and mining depth, larger coal pillars should be designed to support the overburden load. The accuracy of the pillar width should be within 0.2 m to satisfy the engineering requirements. To analyze the abutment stress, the yield zone distribution, and the instability mechanism of the web pillar at different slope angles and mining depths, four modeling schemes are designed. Tables 2, 3, 4 and 5 present the modeling schemes under slope angles of 20°, 30°, 40°, and 50°, respectively. For each scheme, four mining depths are considered, i.e., $l = 50$ m, 65 m, 80 m, and

Table 5 Simulated web pillar widths (m) under different mining depths (m) at slope angle 50°

Mining depth	Pillar width size I	Pillar width size II	Pillar width size III	Pillar width size IV
50	4.3	4.5	4.7	4.9
65	4.7	4.9	5.1	5.3
80	5.1	5.3	5.5	5.7
100	5.6	5.8	6.0	6.2

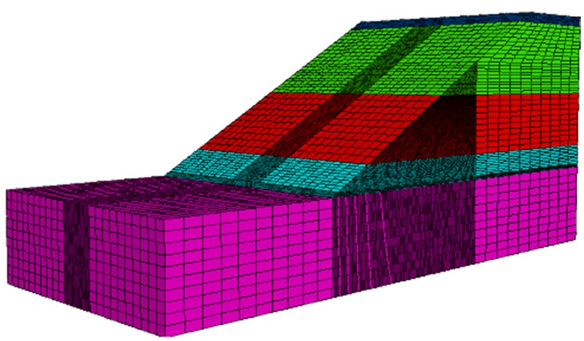

Fig. 3 Numerical model

100 m, and there are four chambers for each mining depth. Each chamber has $h = 2.5$ m and $a = 2$ m, and three web pillars are retained between the chambers. We design four pillar widths for each mining depth, giving a total of 16 simulation models (Fig. 3) in each scheme. Details of the web pillar sizes are listed in Tables 2, 3, 4 and 5.

3.2 Analysis of abutment stress distributions of web pillars

By examining the shear resistance of the web pillars, the abutment stress distribution before pillar failure can be obtained. Analyzing the characteristics of the abutment stress distributions in the web pillar along both the strike direction and the dip direction, the position with the maximum abutment stress under the condition of "triangular loading" is determined. Additionally, the variations in the loading sustained in this position at different slope angles, mining depths, and pillar widths is revealed.

Due to space limitations, this paper only presented the modeling results of the abutment stress distributions for web pillars at a slope angle of 40° (Fig. 4). The engineering positions with the maximum abutment stress under varying pillar widths, mining depths, and slope angles were recorded in Table 6. There is an "end effect" in highwall mining. This is because the stiffness of the web pillar is smaller than the stiffness of the solid slope barrier, which shares some of the overburden load upon the web pillar. The maximum abutment stresses occur somewhere ahead of the web pillars towards the end of chamber excavations. Additionally, the locations of the maximum abutment stresses are not related to the pillar width, but are closely associated with the maximum mining depth and the slope angle (burial depth). Notably, the riskiest web pillar position is at the site where the coal pillar bears the maximum abutment stress. If instability occurs in this position, it may produce a chain reaction and lead to instability of the entire pillar group. The positions with the maximum abutment stress (P_d) are fitted in Fig. 5, and Eq. (1) is derived to demonstrate the relationship between P_d, the slope angle, and the mining depth.

$$P_d = 2.54 - 0.15\theta + 0.9689L \quad (1)$$

where, P_d is the position bearing the maximum abutment stress; θ is the slope angle, and L is the mining depth.

Based on the positions with the maximum abutment stress at different slope angles and mining depths, the stress distributions along the dip direction and the variation of the loading sustained in these positions are studied. In this paper, we only present the results of the stress distributions in the riskiest positions under different pillar widths and mining depths at a slope angle of 40° (Figs. 6 and 7). The results show that the abutment stress is distributed symmetrically along the center of the pillar. As the coal pillar does not break, the stress concentration factor is relatively large at either side of the pillar, but smaller in the center. The stress distribution is approximately bowl-shaped. The maximum and minimum abutment stresses of the web pillars with different widths and mining depths at slope angles of 20°, 30°, 40°, and 50° are recorded in Tables 7, 8, 9 and 10, respectively.

3.3 Analysis of instability mechanism and ultimate strength of web pillars

Based on the distributions of positions at which the maximum abutment stress occurs, namely, the positions at which the web pillars are most vulnerable to instability, the distribution characteristics of the side abutment stress are analyzed under varying pillar widths and mining depths and at slope angles of 20°, 30°, 40°, and 50°. Taking the case of a 40° slope angle for detailed analysis (Figs. 8 and 9), it is evident that, as the pillar width decreases, the stress profile changes from a saddle shape to an approximate platform shape, and finally to an arch shape. Correspondingly, the web pillar undergoes the following evolution process: "stable state–critical equivalent state–ultimate failure state". This is because, with the narrowing of the pillar width, the pillar's ultimate strength decreases as the abutment stress grows. The abutment stress of the web pillar is initially

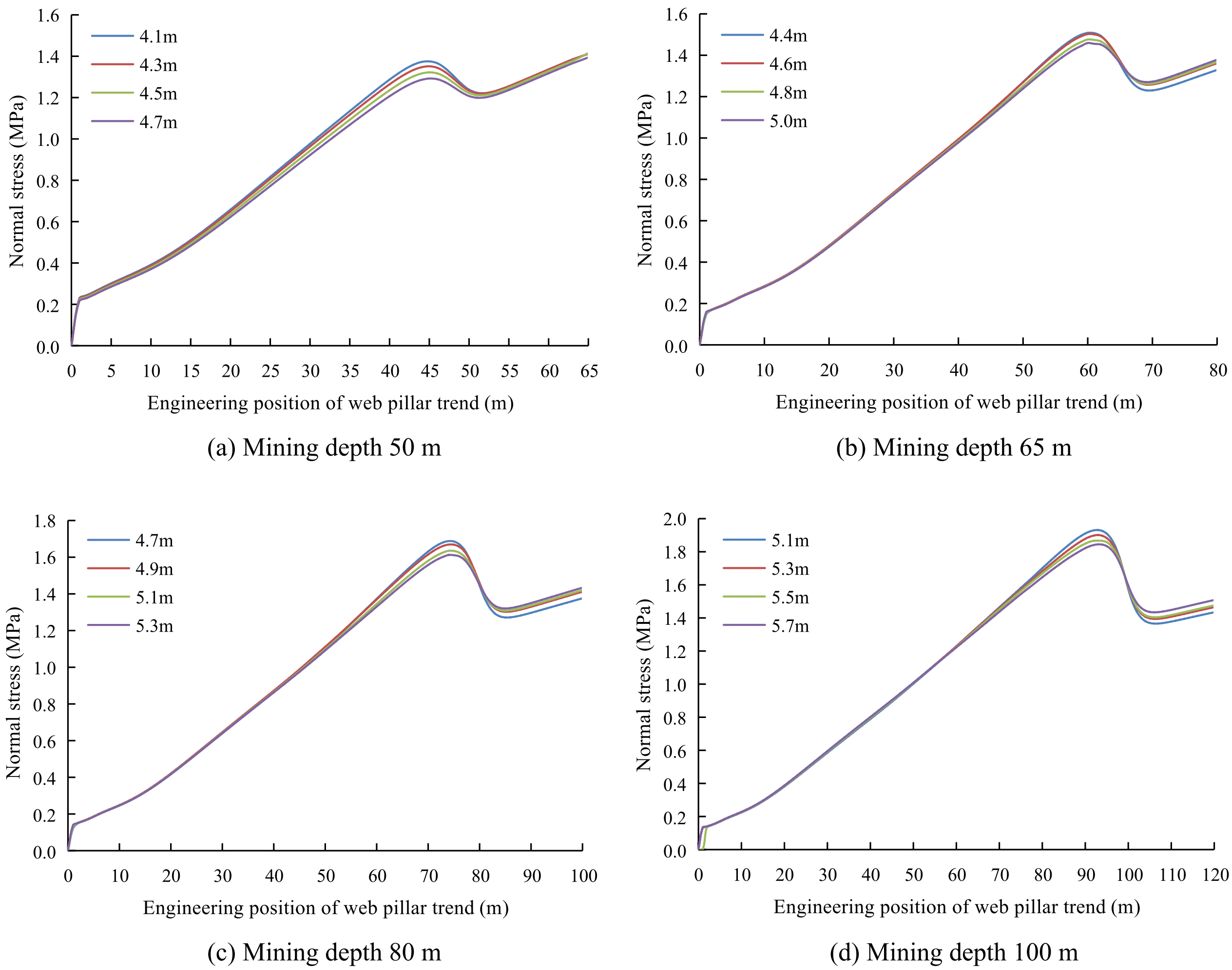

Fig. 4 Abutment stress distributions under different mining widths and pillar sizes at slope angle of 40°

Table 6 Maximum abutment stress positions at different slope angles and mining depths

Slope angle (°)	Mining depth (m)			
	50	65	80	100
20	47	62	78	97
30	46	61	76	95
40	45	60	74	93
50	44	59	72	91

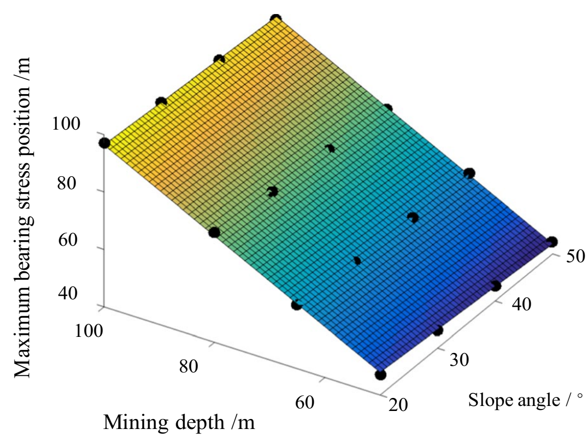

Fig. 5 Fitted maximum abutment stress positions at different slope angles and mining depths

smaller than the pillar's ultimate strength (Fig. 8a) and then becomes equal to the pillar strength (Fig. 8b), implying that the web pillar is in a stable state. Finally, the abutment stress becomes larger than the ultimate strength of the coal pillar (Fig. 8c, d), suggesting that the web pillar is damaged. According to the limit equilibrium theory (Xiong et al. 2019), the ultimate strength of the web pillar can be determined as a function of its width. Under different slope angles and mining depths, web pillars with the same width have almost the same ultimate strength, indicating that the ultimate strength is independent of the slope angle and the mining depth, but is positively correlated with the pillar

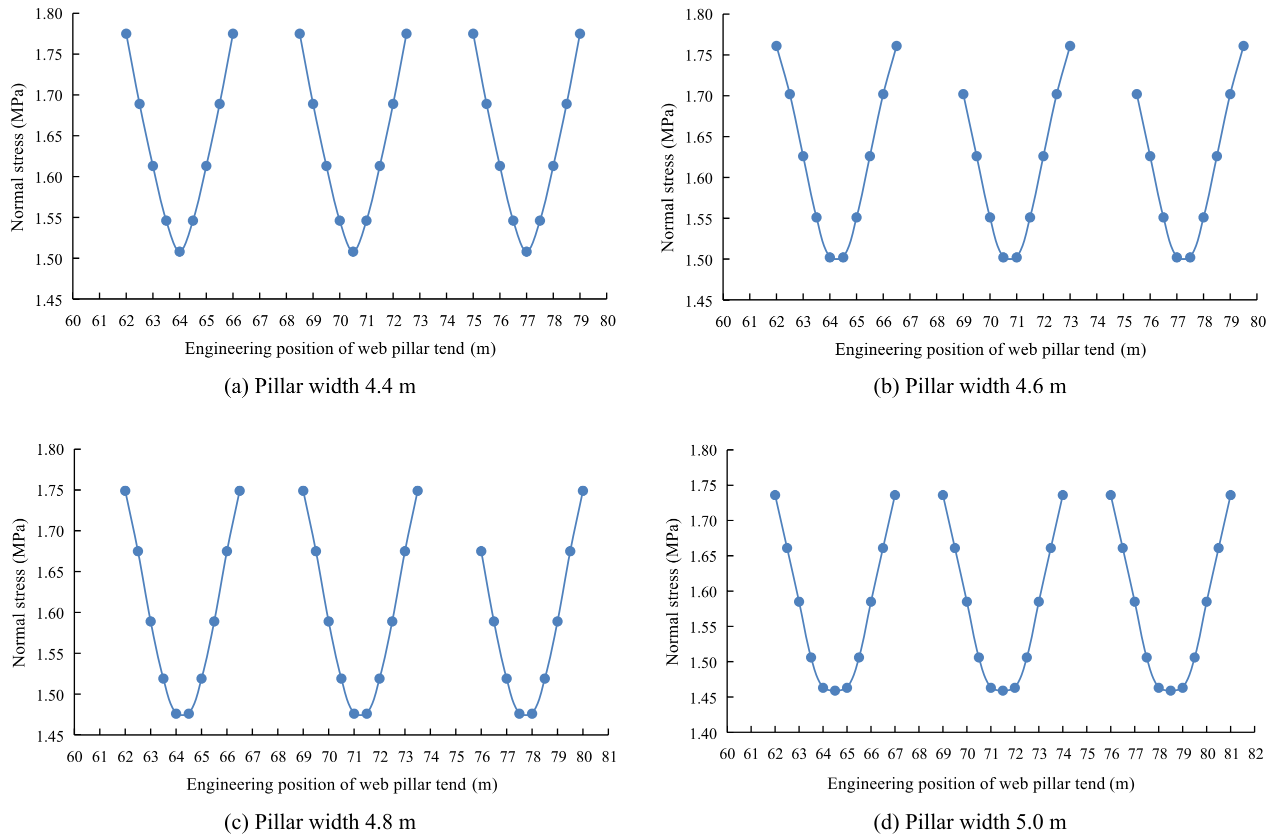

Fig. 6 Side abutment stress distributions for different pillar widths at slope angle 40° and depth 65 m

width. That is, the larger the pillar width, the greater will be the pillar's ultimate strength, as illustrated in Fig. 10.

3.4 Analysis of yield zone distribution

The modeling results of the yield zone distribution in web pillars at different mining depths and a slope angle of 40° are now analyzed in detail (Figs. 11, 12, 13, 14). The results show that the failure pattern of the web pillars is shear failure. If the web pillar has a small width, failure occurs when the yield zones at either side of the web pillar merge with each other (Fig. 11a, b). As the pillar width increases, an elastic core zone (Fig. 11c, d) appears in the center of the web pillar and the yield zones do not meet, implying that the web pillar is in a stable state. The modeling results of the web pillar stability are consistent with the previous analysis of the state identification of web pillars based on the abutment stress distribution. By combining the relationship between the abutment stress and the ultimate strength of the web pillar with the failure characteristics of the yield zones, the instability mechanism of the web pillar in highwall mining can be determined, that is, when the abutment stress of the web pillar exceeds its ultimate strength, shear failure occurs. To improve the recovery rate, the appropriate retaining widths for web pillars under different slope angles and mining depths are identified in Table 11.

4 Instability criterion of web pillars

4.1 Cusp catastrophe model of web pillars

The maximum abutment stress positions of web pillars under the "triangular loading" effect are different from those under a uniform distribution of the overburden rock. The modeling results of the abutment stress distributions indicate that the abutment stress in the riskiest position along the dip direction has a bowl-shaped distribution, rather than the uniform distribution described by effective region theory. Accordingly, a bearing model of the web pillar is established (Fig. 15). The arch-shaped solid curve in the model illustrates the actual distribution of the abutment stress, which is symmetrically distributed along the center of the web pillar. Provided that the actual stress curve follows the two broken lines in the figure, the overburden load of the web pillar (P) can be calculated by Eq. (2).

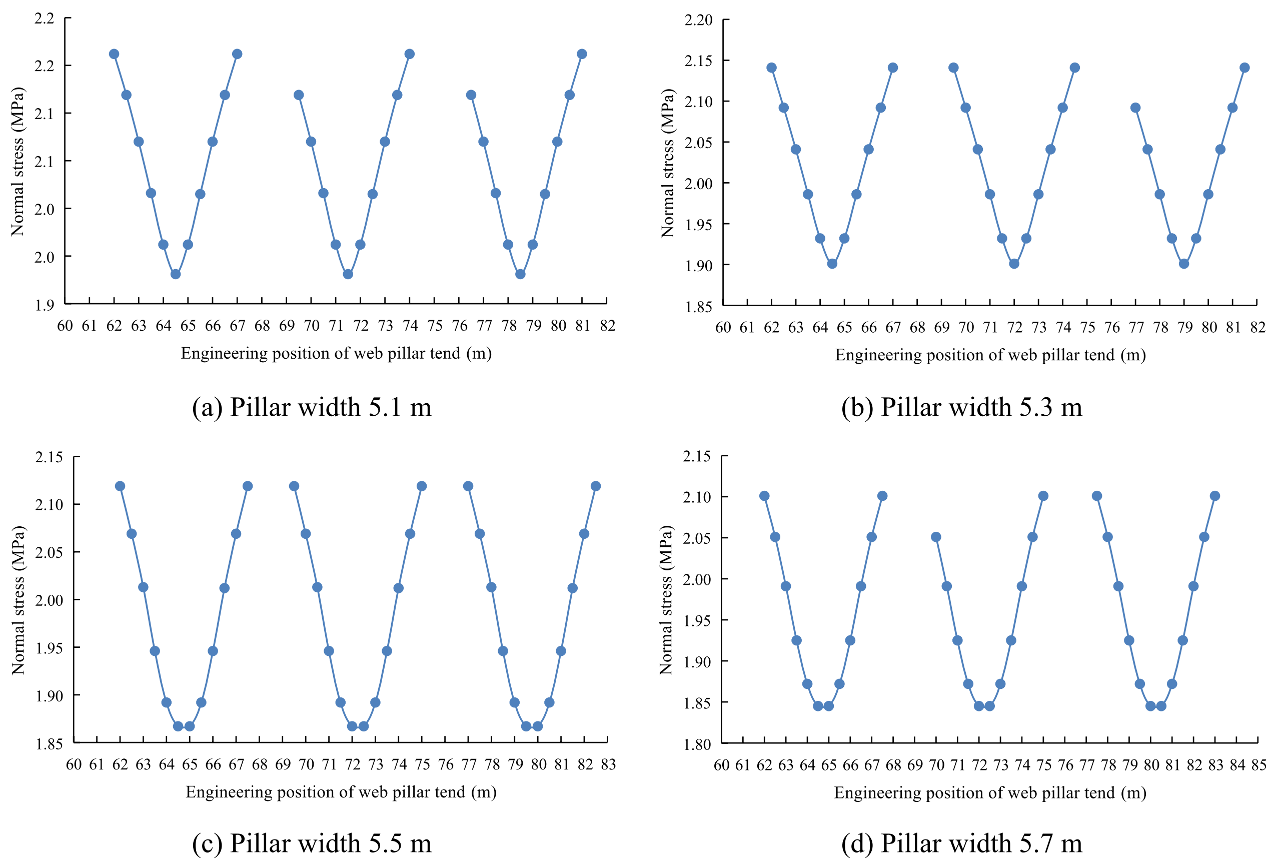

Fig. 7 Side abutment stress distributions for different pillar widths at slope angle 40° and depth 100 m

Table 7 Maximum and minimum bearing stress values of different pillar widths at slope angle 20°

Depth (m)	3.7 m		3.9 m		4.1 m		4.3 m		3.8 m		4.0 m		4.2 m		4.4 m	
	σ_{min}	σ_{max}	σ_{min}	σ_{max}	σ_{min}	σ_{max}	σ_{min}	σ_{max}	σ_{min}	σ_{max}	σ_{min}	σ_{max}	σ_{min}	σ_{max}	σ_{min}	σ_{max}
50	1.179	1.406	1.151	1.389	1.121	1.376	1.101	1.363								
65									1.235	1.466	1.208	1.452	1.181	1.439	1.169	1.428
Depth (m)	3.9 m		4.1 m		4.3 m		4.5 m		4.1 m		4.3 m		4.5 m		4.7 m	
	σ_{min}	σ_{max}	σ_{min}	σ_{max}	σ_{min}	σ_{max}	σ_{min}	σ_{max}	σ_{min}	σ_{max}	σ_{min}	σ_{max}	σ_{min}	σ_{max}	σ_{min}	σ_{max}
80	1.262	1.515	1.239	1.501	1.211	1.489	1.193	1.476								
100									1.377	1.605	1.343	1.591	1.312	1.580	1.282	1.569

Table 8 Maximum and minimum bearing stress values of different pillars widths at slope angle 30°

Depth (m)	3.9 m		4.1 m		4.3 m		4.5 m		4.1 m		4.3 m		4.5 m		4.7 m	
	σ_{min}	σ_{max}	σ_{min}	σ_{max}	σ_{min}	σ_{max}	σ_{min}	σ_{max}	σ_{min}	σ_{max}	σ_{min}	σ_{max}	σ_{min}	σ_{max}	σ_{min}	σ_{max}
50	1.266	1.513	1.239	1.501	1.217	1.486	1.183	1.469								
65									1.386	1.625	1.366	1.611	1.332	1.596	1.315	1.582
Depth (m)	4.3 m		4.5 m		4.7 m		4.9 m		4.6 m		4.8 m		5.0 m		5.2 m	
	σ_{min}	σ_{max}	σ_{min}	σ_{max}	σ_{min}	σ_{max}	σ_{min}	σ_{max}	σ_{min}	σ_{max}	σ_{min}	σ_{max}	σ_{min}	σ_{max}	σ_{min}	σ_{max}
80	1.498	1.728	1.475	1.715	1.449	1.701	1.429	1.686								
100									1.638	1.869	1.613	1.851	1.573	1.835	1.533	1.811

Table 9 Maximum and minimum bearing stress values of different pillars widths at slope angle 40°

Depth (m)	4.1 m		4.3 m		4.5 m		4.7 m		4.4 m		4.6 m		4.8 m		5.0 m	
	σ_{min}	σ_{max}	σ_{min}	σ_{max}	σ_{min}	σ_{max}	σ_{min}	σ_{max}	σ_{min}	σ_{max}	σ_{min}	σ_{max}	σ_{min}	σ_{max}	σ_{min}	σ_{max}
50	1.375	1.622	1.351	1.608	1.322	1.591	1.292	1.575								
65									1.508	1.775	1.502	1.761	1.476	1.749	1.459	1.736
Depth (m)	4.7 m		4.9 m		5.1 m		5.3 m		5.1 m		5.3 m		5.5 m		5.7 m	
	σ_{min}	σ_{max}	σ_{min}	σ_{max}	σ_{min}	σ_{max}	σ_{min}	σ_{max}	σ_{min}	σ_{max}	σ_{min}	σ_{max}	σ_{min}	σ_{max}	σ_{min}	σ_{max}
80	1.688	1.931	1.669	1.915	1.635	1.899	1.612	1.866								
100									1.931	2.162	1.901	2.141	1.867	2.119	1.845	2.101

Table 10 Maximum and minimum bearing stress values of different pillars widths at slope angle 50°

Depth (m)	4.3 m		4.5 m		4.7 m		4.9 m		4.7 m		4.9 m		5.1 m		5.3 m	
	σ_{min}	σ_{max}	σ_{min}	σ_{max}	σ_{min}	σ_{max}	σ_{min}	σ_{max}	σ_{min}	σ_{max}	σ_{min}	σ_{max}	σ_{min}	σ_{max}	σ_{min}	σ_{max}
50	1.492	1.729	1.466	1.713	1.432	1.698	1.413	1.685								
65									1.689	1.925	1.662	1.908	1.635	1.892	1.603	1.877
Depth (m)	5.1 m		5.3 m		5.5 m		5.7 m		5.6 m		5.8 m		6.0 m		6.2 m	
	σ_{min}	σ_{max}	σ_{min}	σ_{max}	σ_{min}	σ_{max}	σ_{min}	σ_{max}	σ_{min}	σ_{max}	σ_{min}	σ_{max}	σ_{min}	σ_{max}	σ_{min}	σ_{max}
80	1.939	2.158	1.902	2.146	1.871	2.132	1.846	2.119								
100									2.292	2.539	2.271	2.522	2.239	2.501	2.210	2.479

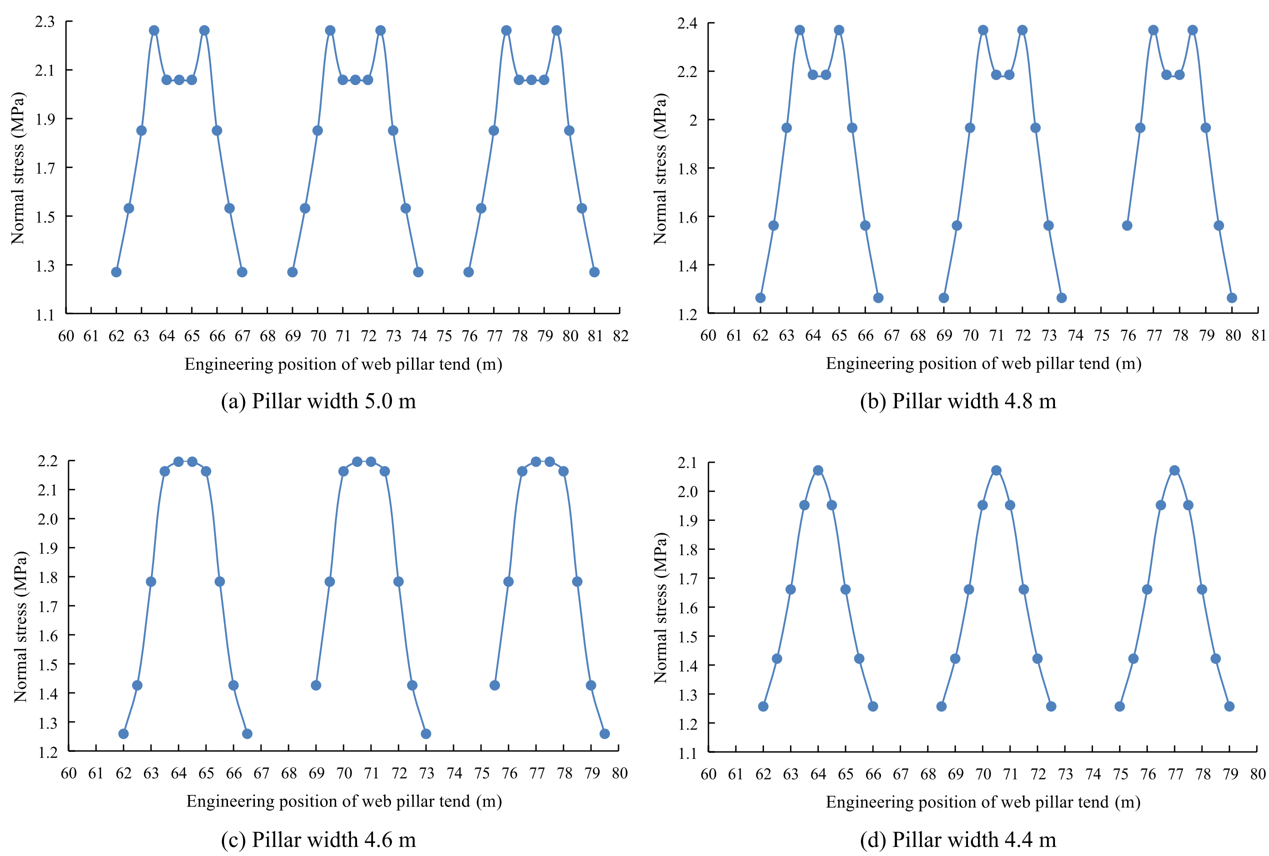

Fig. 8 Side abutment stress distributions for different pillar widths at slope angle 40° and depth 65 m

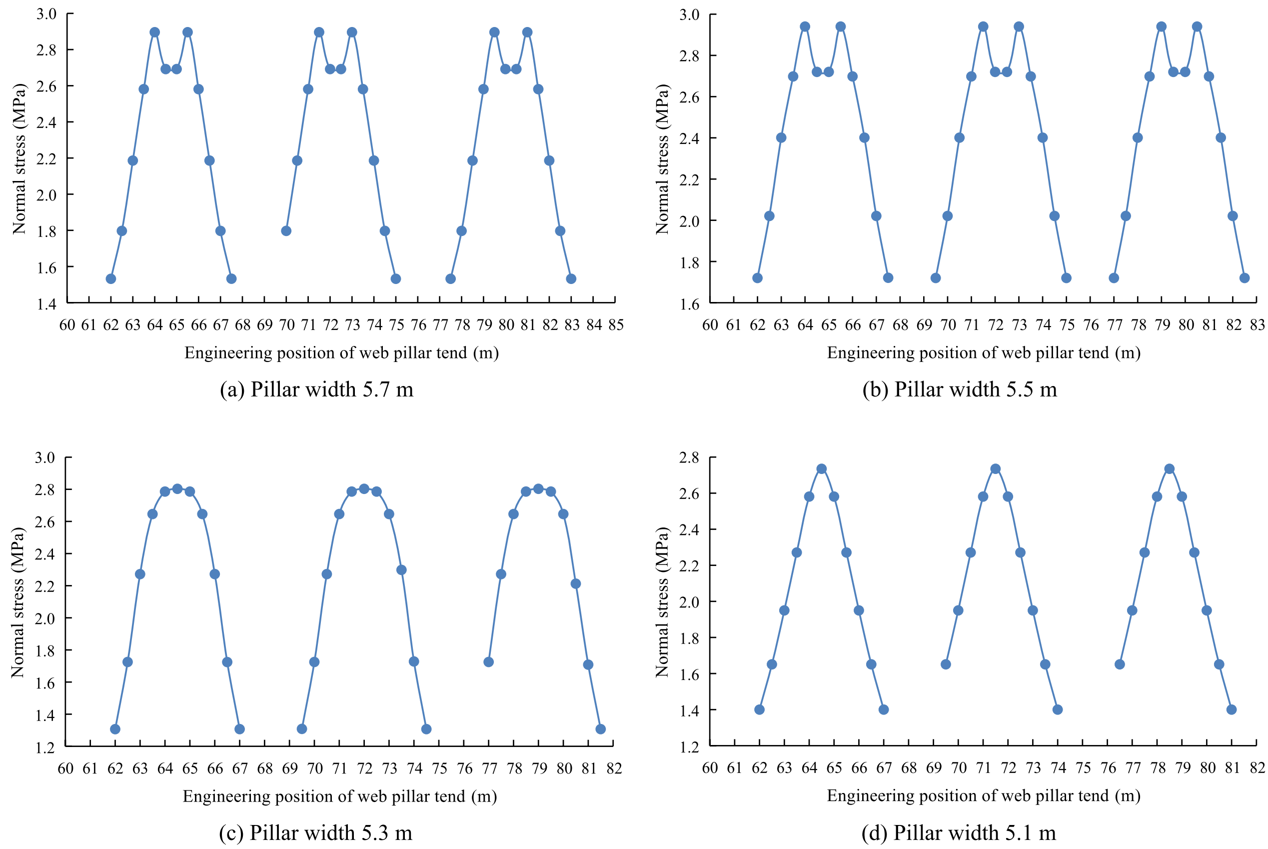

Fig. 9 Side abutment stress distributions for different pillar widths at slope angle 40° and depth 100 m

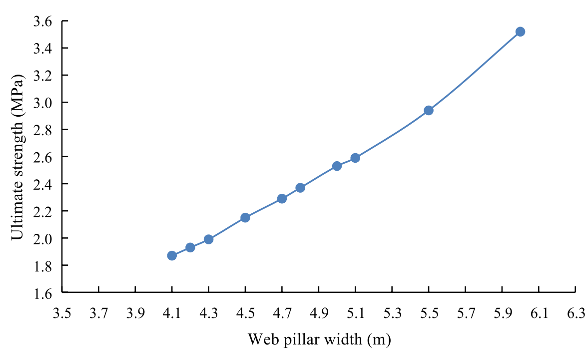

Fig. 10 Ultimate strengths of coal pillars with different widths

$$P = \frac{\sigma_{\min} + \sigma_{\max}}{2} w_s \tag{2}$$

where, $\sigma_{\min}$ is the minimum abutment stress; $\sigma_{\max}$ is the maximum abutment stress, and w_s is the pillar width.

By substituting the maximum and minimum abutment stress values in Tables 7, 8, 9 and 10 into Eq. (2), the overburden load of the web pillar can be calculated for different pillar widths, mining depths, and slope angles. Equation (3) describes the best-fit curve of the bearing stress of the web pillar with respect to the slope angle, mining depth, and pillar width:

$$P = 0.0638\theta + 0.0023L^2 + 0.195w_s^2 \tag{3}$$

Mining activities induce stress redistribution and an overburden load concentrated in the coal pillar, forming symmetrical yield zones at either side of the pillar. Let the yield zone width and the chamber width be denoted by x_p and w_m, respectively. The constitutive relation of the elastic core zone is different from that of the yield zone (Guo et al. 2005) (Fig. 16), and exhibits linearity in the elastic core zone. The coal pillar in the elastic core zone has high strength, conforming to elasticity theory, and has the elastic or strain-hardening property. However, in the yield zone, the constitutive relation curve is nonlinear and has the strain-softening property. Once the coal pillar reaches its peak strength, it will release stress quickly and the pillar strength will drop rapidly, resulting in reduced ability to resist deformation as the deformation grows.

The relationship between the stress of the coal pillar (σ), the strain (ε), and the damage parameter (D) can be expressed as follows (Guo et al. 2004):

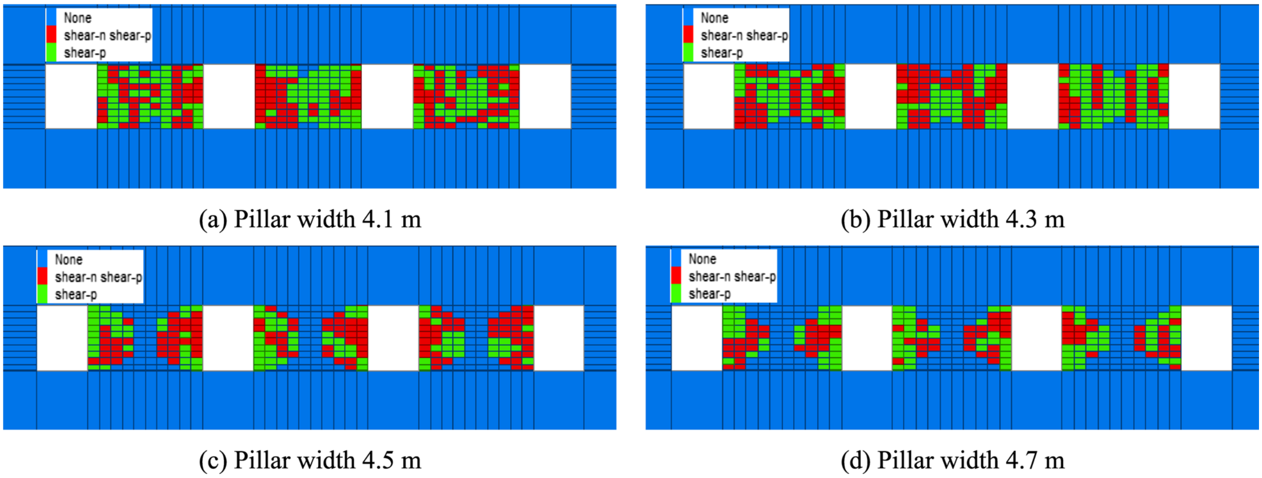

Fig. 11 Yield zone distributions of web pillars with different widths at slope angle 40° and depth 50 m

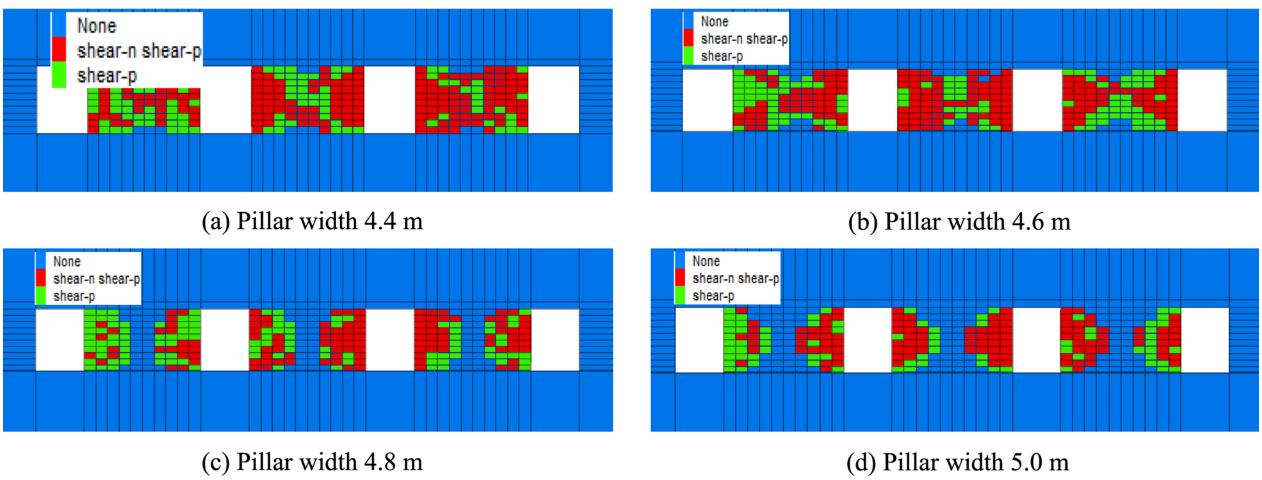

Fig. 12 Yield zone distributions of web pillars with different widths at slope angle 40° and depth 65 m

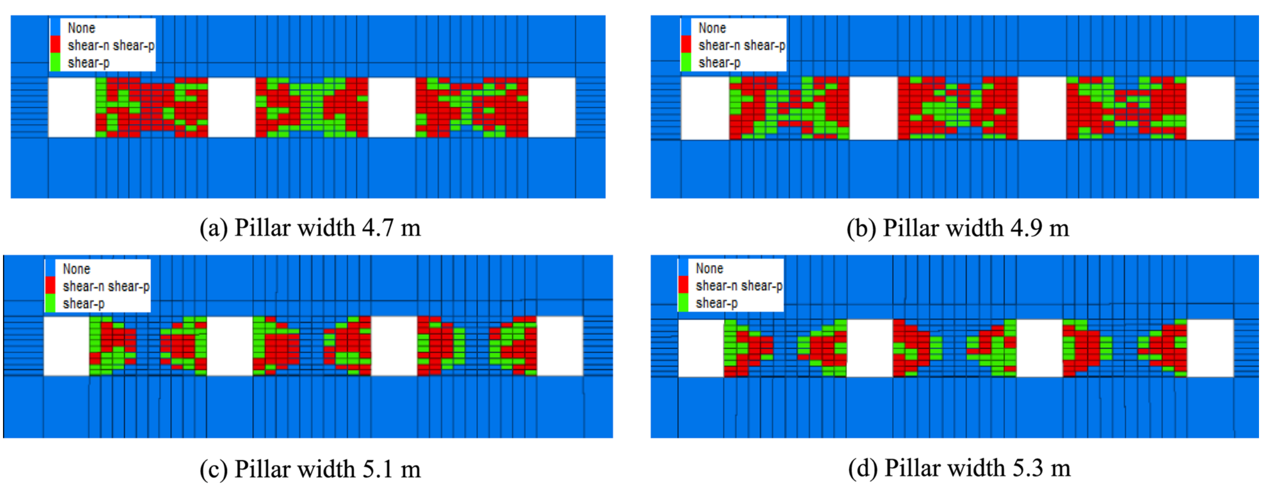

Fig. 13 Yield zone distributions of web pillars with different widths at slope angle 40° and depth 80 m

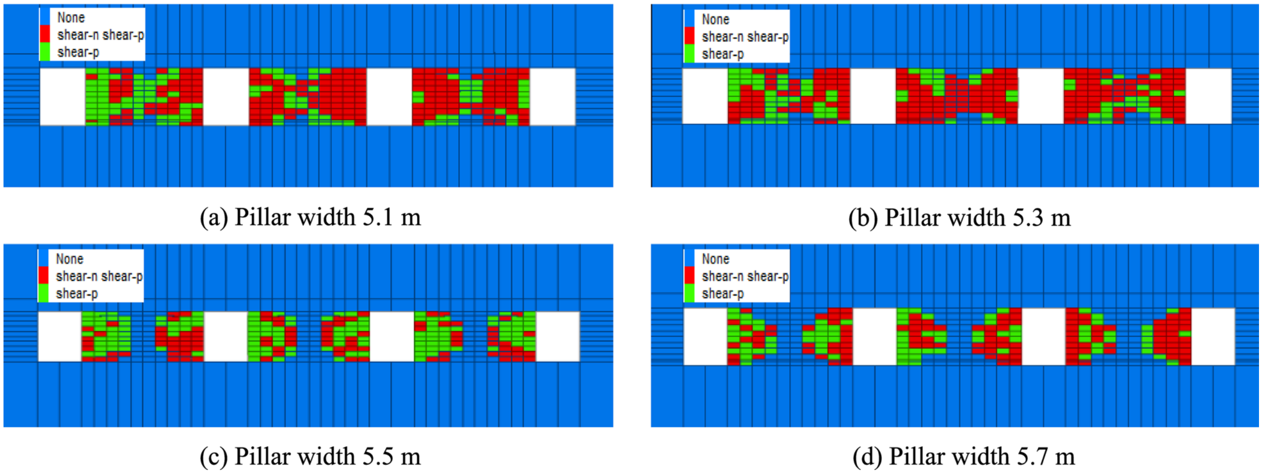

Fig. 14 Yield zone distributions of web pillars with different widths at slope angle 40° and depth 100 m

Table 11 Retaining widths of web pillars at different slope angles and mining depths

Mining depth (m)	Slope angle (°)			
	20	30	40	50
50	4.1	4.3	4.5	4.7
65	4.2	4.5	4.8	5.1
80	4.3	4.7	5.1	5.5
100	4.5	5.0	5.5	6.0

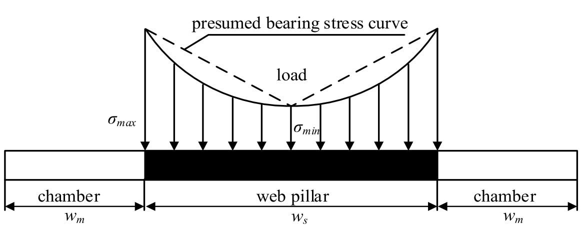

Fig. 15 Bearing model of web pillar

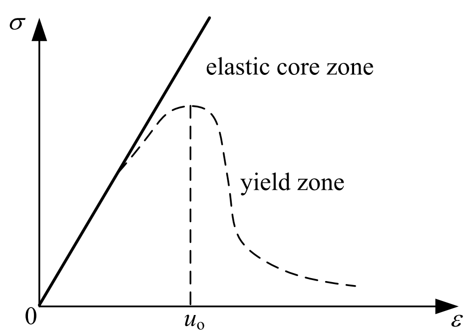

Fig. 16 Constitutive relation curves of the coal pillar

$$\sigma = E\varepsilon(1 - D) \tag{4}$$

where, $D = 1 - \exp\left(-\frac{\varepsilon}{\varepsilon_0}\right)$; ε_0 is the strain variable of the coal pillar under a certain load, and E is the elasticity modulus of the coal pillar.

The yield zones have a total width of $2x_p$, and the coal seam thickness is h. Hence, the relation between the bearing stress in the yield zones (P_s) and the deformation value in these zones (u) can be described as:

$$P_s = \frac{2x_p Eu}{h} \exp\left(-\frac{u}{u_0}\right) \tag{5}$$

where, u_0 is the deformation value of the coal pillar under the maximum bearing stress, $u_0 = \sigma_c h/E$.

The width of the elastic core zone is $w_s - 2x_p$, which conforms to the elasticity principle. The corresponding bearing stress in this zone is given by:

$$P_e = \frac{Eu}{h}\left(w_s - 2x_p\right) \tag{6}$$

Thus, the strain energy (V_s) and the elastic potential energy (V_e) of the coal pillar in the yield zones and the elastic core zone can be written as:

$$V_s = \frac{2Ex_p}{h} \int_0^u \exp\left(-\frac{u}{u_0}\right) \mathrm{d}u \tag{7}$$

$$V_e = \frac{2E\left(w_s - 2x_p\right)}{h} \int_0^u u\mathrm{d}u \tag{8}$$

The potential energy of the overburden (V_p) is expressed as follows:

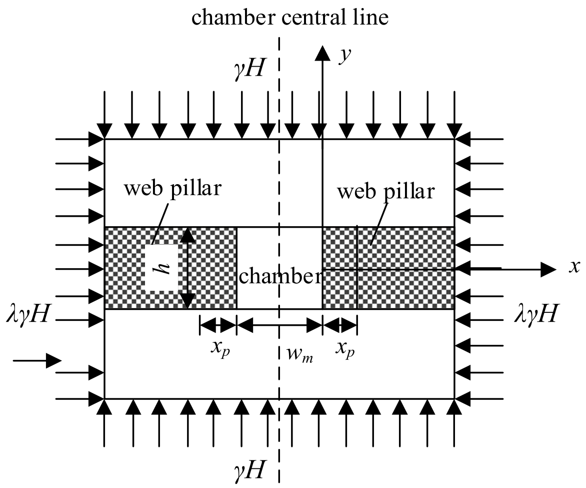

Fig. 17 Mechanical model of chamber and surrounding rocks

$$V_{\mathrm{p}} = \left(0.0638\theta + 0.0023L^2 + 0.195w_{\mathrm{s}}^2\right)u \tag{9}$$

The total potential energy function in the mechanical model shown in Fig. 17 can be calculated by:

$$V = \frac{2Ex_{\mathrm{p}}}{h}\int_0^u u\left(-\frac{u}{u_0}\right)\mathrm{d}u + \frac{2E\left(w_{\mathrm{s}} - 2x_{\mathrm{p}}\right)}{h}\int_0^u u\mathrm{d}u - \left(0.0638\theta + 0.0023L^2 + 0.195w_{\mathrm{s}}^2\right)u \tag{10}$$

Here, u is considered as the state variable for analysis using cusp catastrophe theory. Setting the first derivative of V equal to zero (i.e., $V'=0$), the equation for the equilibrium surface (M) can be derived as:

$$V' = \frac{2Ex_{\mathrm{p}}}{h}u\exp\left(-\frac{u}{u_0}\right) + \frac{E\left(w_{\mathrm{s}} - 2x_{\mathrm{p}}\right)}{h}u - 0.0638\theta - 0.0023L^2 - 0.195w_{\mathrm{s}}^2 = 0 \tag{11}$$

Equation (11) is the equilibrium condition of the mechanical model. To establish the cusp catastrophe model, we take the derivative of the equilibrium surface equation and set the second derivative (i.e., V'') equal to zero:

$$V'' = 2\left(w_{\mathrm{s}} - x_{\mathrm{p}}\right)x_{\mathrm{p}}\frac{E}{u_0}\left(2 - \frac{u}{u_0}\right) + \left(-4w_{\mathrm{s}}x_{\mathrm{p}} + 2w_{\mathrm{s}}x_{\mathrm{p}}\frac{u}{u_0} + 4x_{\mathrm{p}}^2 - 2x_{\mathrm{p}}^2\frac{u}{u_0}\right)\left(\frac{1}{u_0}\right)e^{-\frac{u}{u_0}} = 0 \tag{12}$$

The solution of $V''=0$ is $u=u_1=2u_0$. Expanding Eq. (12) about $u=u_1=2u_0$ according to Taylor's formula and neglecting powers above the cubic term, we have:

$$\frac{4x_{\mathrm{p}}Eu_1e^{-2}}{3h}\left\{\left(\frac{u-u_1}{u_1}\right)^3 + \frac{3\left(u-u_1\right)}{2u}\left[\frac{\left(w_{\mathrm{s}} - 2x_{\mathrm{p}}\right)e^2}{2x_{\mathrm{p}}} - 1\right] + \frac{3}{2}\left[1 + \frac{\left(w_{\mathrm{s}} - 2x_{\mathrm{p}}\right)e^2}{2x_{\mathrm{p}}} - \frac{Phe^2}{2x_{\mathrm{p}}Eu_1}\right]\right\} = 0 \tag{13}$$

Let the dimensionless quantity z be the state variable, and let p and q be the control variables:

$$z = \frac{u-u_1}{u_1}, \quad p = \frac{3}{2}\left(k_0 - 1\right), \quad q = \frac{3}{2}\left(1 + k_0 - t\right) \tag{14}$$

$$\begin{aligned} k_0 &= \frac{k_{\mathrm{e}}}{k_{\mathrm{s}}} = \frac{E\left(w_{\mathrm{s}} - 2x_{\mathrm{p}}\right)/h}{2x_{\mathrm{p}}Ee^{-2}/h} = \frac{\left(w_{\mathrm{s}} - 2x_{\mathrm{p}}\right)e^2}{2x_{\mathrm{p}}}, \\ t &= \frac{he^2}{2x_{\mathrm{p}}Eu_1}\left(0.0638\theta + 0.0023L^2 + 0.195w_{\mathrm{s}}^2\right) \end{aligned} \tag{15}$$

where, k_{e} and k_{s} are the material stiffness in the elastic core zone and in the yield zone, respectively; t is a parameter related to highwall mining conditions, that is, it is relevant to the mining height, retaining width, mining depth, overburden bulk density, coal deformation parameter, and other factors.

According to Eqs. (13)–(15), the standard equilibrium equation of the cusp catastrophe model is obtained as:

$$z^3 + pz + q = 0 \tag{16}$$

The derivative of Eq. (16) gives the singular point equation of the system:

$$3z^2 + p = 0 \tag{17}$$

Combining Eqs. (16) and (17), the bifurcation set equation of the system can be obtained as:

$$\Delta = 8p^3 + 27q^2 = 0 \tag{18}$$

Substituting Eq. (14) into Eq. (18), we obtain the simplified expression:

$$\Delta = 2\left(k_0 - 1\right)^3 + 9\left(1 + k_0 - t\right)^2 = 0 \tag{19}$$

Finally, substituting Eq. (15) and $u_0 = \sigma_c h/E$ into Eq. (19), we obtain the following fitted expression:

$$\Delta = 2\left[\frac{\left(w_s - 2x_p\right)e^2}{2x_p} - 1\right]^3 + 9\left[1 + \frac{\left(w_s - 2x_p\right)e^2}{2x_p} - \frac{e}{4x_p\sigma_c}\left(0.0638\theta + 0.0023L^2 + 0.195w_s^2\right)\right]^2 = 0 \tag{20}$$

A value of $\Delta > 0$ means the system is in a stable state, and $\Delta = 0$ implies the system is in the critical equilibrium state. Only when $\Delta < 0$ can the system cross the bifurcation set and fail instantly. Therefore, the sufficient and necessary conditions for the instability catastrophe of coal pillars are as follows:

$$2[\frac{\left(w_s - 2x_p\right)e^2}{2x_p} - 1]^3 + 9\left[1 + \frac{\left(w_s - 2x_p\right)e^2}{2x_p} - \frac{e^2}{4x_p\sigma_c}(0.0638\theta + 0.0023L^2 + 0.195w_s^2)\right]^2 < 0 \tag{21}$$

4.2 Yield zone width calculation

In view of the problems with the classical elastic–plastic analysis of rock mechanics, and based on limit equilibrium theory, it is further assumed that the coal seam roof and floor have the same lithology and have greater strength than the coal (Wilson et al. 1973). A mechanical model (Gu et al. 2014, 2015) of the chamber and the surrounding rock is established without considering the body force (Fig. 17).

As the yield zone is the limit equilibrium zone, the shear stress τ and the vertical stress σ_y at the interface between the coal seam roof and floor satisfy the following conditions:

$$\tau = c_0 + \sigma_y \tan\varphi_0 \tag{22}$$

where, c_0 and φ_0 are the internal friction angle and the cohesion of the coal seam interface. The equilibrium equation in the x-direction is established as:

$$h\sigma_x + 2\pi \mathrm{d}x - h\left(\sigma_x + \frac{\partial\sigma_x}{\partial x}\mathrm{d}\sigma_x\right) = 0 \tag{23}$$

According to the Mohr–Coulomb failure criterion, when the yield zone of the coal body is in the limit equilibrium state, we have:

$$\sigma_1 = \frac{1+\sin\varphi}{1-\sin\varphi}\sigma_3 + \frac{2c\cos\varphi}{1-\sin\varphi} \tag{24}$$

Given the assumed symmetry of the problem, the vertical and horizontal stresses in the x-axis are the principal stresses. In Eq. (24), $\sigma_1 = \sigma_y$, $\sigma_3 = \sigma_x$, c is the internal friction angle, and φ is the cohesion of the coal body. Taking the derivative of Eq. (24), the following expression is obtained:

$$\frac{\partial\sigma_y}{\partial x} = \frac{1+\sin\varphi}{1-\sin\varphi}\frac{\partial\sigma_x}{\partial x} \tag{25}$$

If $A = (1+\sin\varphi)/(1-\sin\varphi)$, then

$$\frac{\partial\sigma_y}{\partial x} = A\frac{\partial\sigma_x}{\partial x} \tag{26}$$

Substituting Eq. (26) into Eq. (24), we derive the following expression:

$$\frac{\partial\sigma_y}{\partial x} - \frac{2A\tan\varphi_0}{h}\sigma_y = \frac{2c_0 A}{h} \tag{27}$$

Considering the boundary condition $\sigma_{x=0} = 0$ and setting $N = (2c\cos\varphi)/(1+\sin\varphi)$, the vertical stress and the horizontal stress in the x-axis of the yield zone can be deduced as:

$$\begin{cases} \sigma_y^p = \left(NA + \frac{c_0}{\tan\varphi_0}\right)e^{\frac{2A\tan\varphi_0}{h}x} - \frac{c_0}{\tan\varphi_0} \\ \sigma_x^P = \left(N + \frac{c_0}{A\tan\varphi_0}\right)(e^{\frac{2A\tan\varphi_0}{h}x} - 1) \end{cases} (0 \le x \le x_p) \tag{28}$$

In combination with stress balance theory, after the chamber has been excavated, the load imposed on the original coal body along the length of the chamber is transferred to the adjacent coal body. Provided that the vertical stress and the horizontal stress in the x-axis are equal to the average stress along the height of the coal seam, and according to the assumption of symmetry, the following equation can be obtained:

$$\frac{w_m}{2}\gamma H = \int_0^{x_p}(\sigma_y^p - \gamma H)\mathrm{d}x + \int_{x_p}^{+\infty}(\sigma_y^e - \gamma H)\mathrm{d}x \tag{29}$$

Integrating both sides of Eq. (29), if $X = 2A\tan\varphi_0 x_p h$, then $x_p = Xh2A\tan\varphi_0$, and:

Table 12 Instability criteria for coal pillar widths under different slope angles and mining depths

Slope angle (°)	Mining depth (m)	Retaining pillar width (m)	Burial depth (m)	Yield zone width x_p (m)	Instability criterion Δ
20	50	4.1	18.00	1.11	1143
20	65	4.2	23.40	1.16	1244
20	80	4.3	28.80	1.25	1312
20	100	4.5	36.00	1.37	1530
30	50	4.3	29.00	1.26	1401
30	65	4.5	37.70	1.39	1636
30	80	4.7	46.40	1.50	1917
30	100	5.0	58.00	1.63	2527
40	50	4.5	41.50	1.44	1570
40	65	4.8	53.95	1.59	2033
40	80	5.1	66.40	1.72	2676
40	100	5.5	83.00	1.87	3949
50	50	4.7	59.50	1.65	1536
50	65	5.1	77.35	1.82	2232
50	80	5.5	95.20	1.97	3327
50	100	6.0	100.00	2.00	7005

$$\frac{w_m \gamma H A \tan\varphi_0}{h} = \left\{ \left(NA + \frac{c_0}{A\tan\varphi_0} \right)(X+1)e^x - 2\left(\gamma H + \frac{c_0}{\tan\varphi_0} \right) X - \left(NA + \frac{c_0}{\tan\varphi_0} \right) \right\} \tag{30}$$

Rearranging this expression, we have:

$$x_p = \ln\left[\frac{\frac{2(\gamma H \tan\varphi_0 + c_0)}{(NA\tan\varphi_0 + c_0)} X + \frac{w_m \gamma H \tan^2\varphi_0}{h(NA\tan\varphi_0 + c_0)} + 1}{(X+1)} \right] \tag{31}$$

5 Case study

The burial depth of the No. 21 coal seam is $H = 100$ m, the average bulk density of the overlying strata is $\gamma = 23.6$ kN/m^3, the chamber width is $w_m = 2.0$ m, the chamber height is $h = 2.5$ m, the mining depth is 100 m, the cohesion is $c = c_0 = 0.30$ MPa, the internal friction angle is $\varphi = \varphi_0 = 17.6°$, and the compressive strength of the web pillar is $\sigma_c = 17.66$ MPa. Substituting these parameters, along with the depths and retaining pillar widths provided in Table 11, into Eqs. (31) and (21), the yield zone widths at each side of the web pillars and the instability criteria of the web pillars under different slope angles and mining depths are as displayed in Table 12. It can be seen that the instability criteria for the retaining pillar widths are all greater than zero ($\Delta > 0$), implying that the web pillars are in a stable state. Therefore, the designed web pillar widths are reasonable.

6 Conclusions

(1) From the modeling results, the maximum abutment stress in the web pillar along the pillar strike direction is located somewhere ahead of the web pillar towards the maximum mining depth, and the abutment stress distribution along the dip direction is approximately bowl-shaped. By combining the relationship between the abutment stress and the ultimate strength of the web pillar with the failure characteristics of the yield zone, the instability mechanism of the web pillar has been revealed. Specifically, when the abutment stress of the web pillar is greater than its ultimate strength, shear failure occurs. Based on the characteristics of the abutment stress distribution and the yield zone distribution, it is possible to design and evaluate the retaining widths of the web pillars.

(2) According to the characteristics of the abutment stress distributions, a mechanical bearing model of the web pillar has been established. An equation describing the coal pillar load under different slope angles, mining depths, and pillar widths was established by fitting numerical data to a mathematical expression. Based on cusp catastrophe theory, a pillar-overburden model was constructed, and the sufficient and necessary conditions for the web pillar instability were derived.

(3) Using the mechanical model of the chamber and surrounding rock established in this study, the formula for calculating the yield zone width, considering the width of the chamber either side of the web pillar, was obtained. This formula can be used in combination with the instability criterion of web pillars to validate the rationality of the designed pillar widths and provide theoretical guidance on safe mining operations and high recovery efficiency in open-pit highwall mining.

Authors' contributions All authors read and approved the finalmanuscript.

Funding This project was supported by the National Natural Science Foundation of China under Project No. 51874160, LNTU20TD-01, and the "Millions of Talents Project" of Liaoning Province China.

References

Bieniawski ZT et al (1968) The effect of specimen size on compressive strength of coal. Int J Rock Mech Min Sci Geomech Abst 5(4):325–326

Bunting D et al (1911) Chamber pillars in deep anthracite mines. Trans AIME 42:236–245

Chandar KR, Kumar BG et al (2014) Effect of width of gallery of highwall mining on stability of highwall: a numerical modelling approach. Int J Min Miner Eng 5(3):212–228

Chandar KR, Hegde C, Yellishetty M et al (2015) Classification of stability of highwall during highwall mining: a statistical adaptive learning approach. Geotech Geolog Eng 33:511–521

Deliveris AV, Benardos A (2017) Evaluating performance of lignite pillars with 2D approximation techniques and 3D numerical analyses. Int J Min Sci Technol 27:929–936

Galvin JM, Hebblewhite BK, Salmon MDG et al (1999) University of New South Wales coal pillar strength determinations for Australian and South African mining conditions. In: Proceedings of the 2nd workshop on coal pillar mechanics and design, pp 63–72

Ghaednia H, Wang X, Saha S, Xu Y, Sharma A, Jackson RL et al (2017) A review of elastic-plastic contact mechanics. Appl Mech Rev 69(6):1–29

Greenwald HP, Howarth HC, Hartman I et al (1939) Experiments on strength of small pillars of coal in the Pittsburgh bed. US Bureau of Mines, Washington, p 605

Gu SC, Fan Q, Liu W et al (2015) Study on calculating the width of plastic zone in two sides of rectangular coal drift. Min R D 35(01):60–63

Gu SC, Fan Q, Chen X et al (2014) A calculation method of plastic zone width for rectangular coal roadway. Coal Saf 45(09):24–27, 31

Guo WB, Deng KZ, Zou YF et al (2004) Cusp catastrophic model of instability of strip coal pillar along strike. Chin J Rock Mech Eng 23(12):1996–2000

Guo WB, Deng KZ, Zou YF et al (2005) Study on failure and instability of strip coal pillar by catastrophic theory. J China Univ Min Technol 34(01):80–84

Han XP et al (2014) An unmanned intelligent mining machine. Chinese Patent No. 10123925.5

Hikaru S, Yanlong C, Akihiro H et al (2013) Application of highwall mining system to recover residual coal in end-walls. Procedia Earth Planet Sci 6:311–318

Holland CT, Gaddy FL et al (1957) Some aspects of permanent support of overburden on coal beds. In: Proceedings of the West Virginia coal mining institute, pp 43–65

Holland CT et al (1964) The strength of coal in mine pillars. In: Proceedings of the 6th symposium rock mechanics, pp 450–456

Huang J, Meng FB, Wang G, Wu YK, Wen JH et al (2021) Simulation research for the influence of mining sequence on coal pillar stability under highwall mining method. Geofluids 1–9

Jiang JY, Yang HW, Wang D, Wang LG, Han XP (2021) Experimental study on instability evolution mechanism of rib pillars during highwall mining. China Saf Sci J 31(10):89–96

Lukáš Ď, Richard Š et al (2017) Numerical analysis of the stability of lignite pillars. Procedia Eng 191:310–316

Mo S, Canbulat I, Zhang C, Oh J, Shen B, Hagan P (2018) Numerical investigation into the effect of backfilling on coal pillar strength in highwall mining. Int J Min Sci Technol 28(2):281–286

Porathur JL, Karekal S, Palroy P (2013) Web pillar design approach for Highwall Mining extraction. Int J Rock Mech Min Sci 64:73–83

Ross C, Conover D, Baine J (2019) Highwall mining of thick, steeply dipping coal—a case study in geotechnical design and recovery optimization. Int J Min Sci Technol 29(5):777–780

Salamon MDG, Munro AH et al (1967) A study of the strength of coal pillars. J S Afr Inst Min Metall 68:55–67

Sasaoka T, Karian T, Hamanaka A et al (2016) Application of highwall mining system in weak geological condition. Int J Coal Sci Technol 3(3):311–321

Sheorey PR et al (1992) Pillar strength considering in situ stress. In: Workshop on coal pillar mechanics and design, pp 122–127

Song ZL, Fan JF, Qi WH et al (2016) On the establishment of the evaluation system for green mining in large open-pit coal mines. J Saf Env 41(S2):350–358

Wang R, Yan S, Bai JB, Chang ZG, Song YB et al (2019a) Theoretical analysis & study of the destabilization on damaged width of rib pillar in open-pit highwall mining. Rock Soil Mech 40(8):1–13

Wang FT, Zhang C et al (2019b) Reasonable coal pillar design and remote control mining technology for highwall residual coal resources. R Soc 6(4):1–13

Wang R, Yan S, Bai JB, Chang ZG, Zhao TH et al (2019c) Theoretical analysis of damaged width & instability mechanism of rib pillar in open-pit highwall mining. Adv Civ Eng 1–15

Wilson AH, Sun JL et al (1973) Study on a determining size of the coal. Mine Surv 9(1):30–42

Xiong GJ et al (2019) Limit equilibrium theory of axisymmetric based on rigorous conditions and its application calculation of earth pressure. Shanghai Jiao Tong University, Shanghai

Zhang LY, Deng KZ, Zhu CG, Xing ZQ et al (2011) Analysis of stability of coal pillars with multi-coal seam strip mining. Trans Nonferrous Met Soc China 21(S3):549–555

Zhao HZ, Tian Y, Guo QY, Li MJ, Wu JW (2020a) The slope creep law for a soft rock in an open-pit mine in the Gobi region of Xinjiang. China Int J Coal Sci Technol 7(2):371–379

Zhao HZ, Wang DY, Ma M, Zheng KH (2020b) Parameter inversion and location determination of evolutionary weak layer for open-pit mine slope. Int J Coal Sci Technol 7(4):714–724